High-Frequency Fe-H Vibrations in a Bridging Hydride Complex Characterized by NRVS and DFT

Vladimir Pelmenschikov, Leland B. Gee, Hongxin Wang, K. Cory MacLeod, Sean F. McWilliams, Kazimer L. Skubi, Stephen P. Cramer,* and Patrick L. Holland*

Table of Contents

Experimental Procedures

Preparation of 1 and 1-D$_2$. Compound **1** used for these experiments had iron-57 labeling. It was prepared as described in the literature,[1] but the starting material was ^{57}Fe-labeled FeCl$_2$ that had been prepared from treatment of ^{57}Fe powder (Cambridge Isotopes, 95% isotopic purity) with HCl in methanol. The isotopologue of **1** with deuterium at the bridging positions (**1-D$_2$**) was prepared by addition of 1 atm of D$_2$ to a toluene solution of **1**, which leads to partial deuteration of the hydride positions. Repeating this treatment with D$_2$ three times ensured complete deuteration. The efficacy of the hydride/deuteride exchange was shown by the growth of new peaks in the ^{1}H NMR spectrum corresponding to **1-D$_2$**, and these are shifted from those in **1** and in the singly deuterated **1-D$_1$** because of PIECS (paramagnetic isotope effect on chemical shift).[2] Samples were recrystallized from toluene after this treatment to give purified samples of **1-D$_2$** for further use. The relative intensities of the NMR resonances were unchanged after deuteration, indicating that none of the deuterium atoms exchange into the supporting ligands. The same isotopic substitution with D$_2$ gas occurs with other diketiminate-supported iron-hydride complexes.[2b]

Spectroscopy

Figure S1. ^{1}H NMR spectra of **1** and **1-D$_2$** in C$_6$D$_6$.

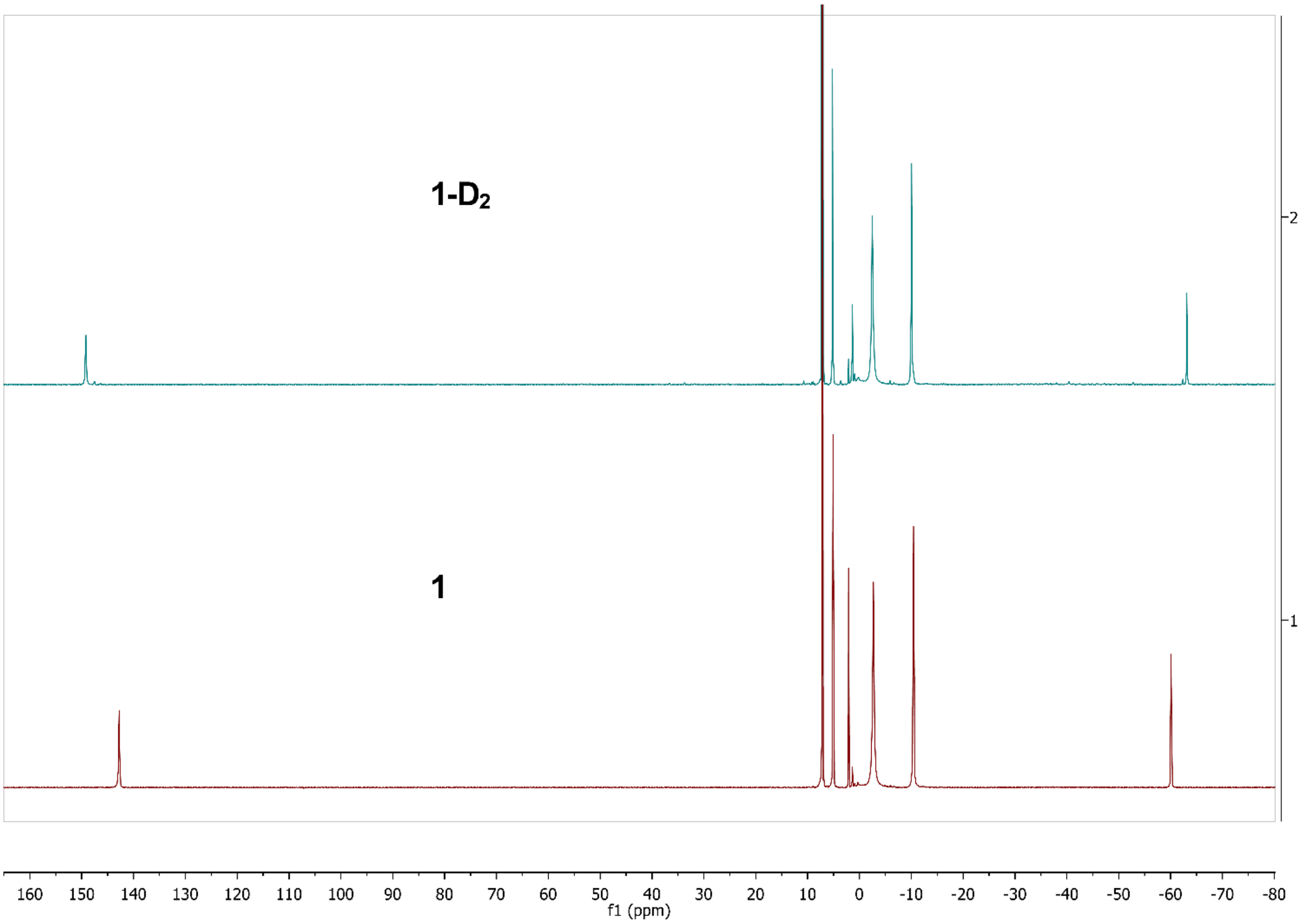

Figure S2. IR data were recorded on a Bruker ALPHA spectrometer equipped with a Platinum-ATR attachment. The blue spectrum corresponds to **1**, and the red spectrum to **1-D$_2$.** The positions of the observed NRVS bands for **1** and **1-D$_2$** are shown using blue and red arrows, correspondingly; it is evident that IR bands in these positions are unobservable.

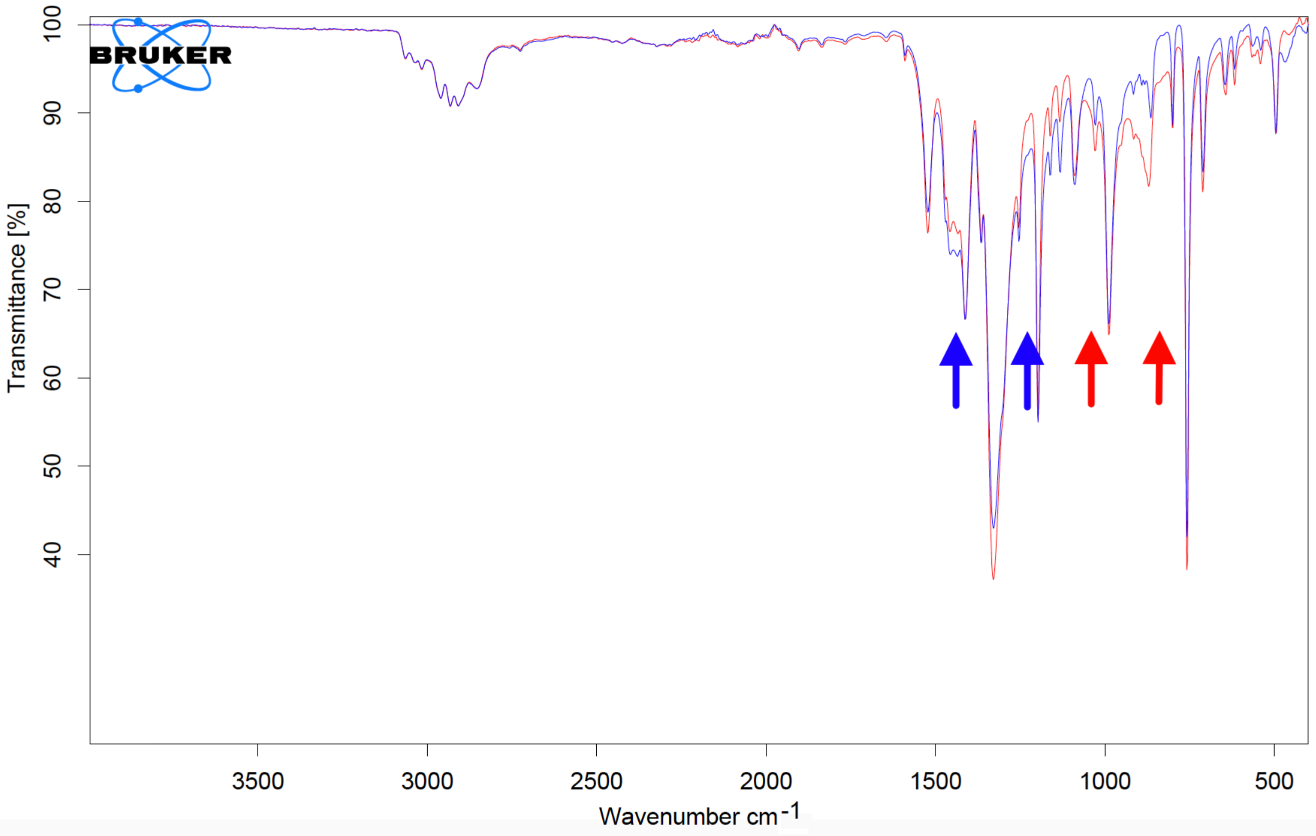

Mössbauer Spectra. Mössbauer data of solid samples with natural-abundance Fe (~2% ^{57}Fe) were recorded on a SEECo spectrometer with alternating constant acceleration; isomer shifts are relative to iron metal at 298 K. The sample temperature was maintained in a Janis Research Company Inc. cryostat. The zero-field spectra were simulated using Lorentzian doublets using WMoss (SeeCo).

Figure S3. Mössbauer spectra of natural-abundance solid samples of **1** (left) and **1-D$_2$** (right) at 170 K.

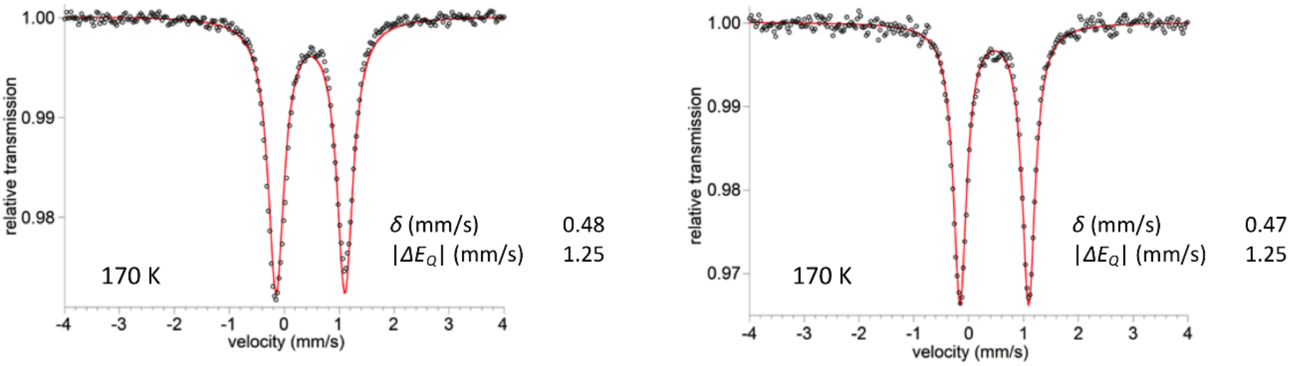

At lower temperature, there is a phase change in the crystals, which leads to splitting in the Mössbauer spectra that suggests a loss of the symmetry operation that relates the sites. The nature of this temperature-dependent transition is not yet understood and is under investigation. The transition is not observed in frozen solutions, and therefore it is a phase change connected with the solid-state packing. Accordingly, the desymmetrization was not observed in the DFT optimized structures (see below).

Figure S4. Mössbauer spectra of natural-abundance solid samples of **1** (left) and **1-D$_2$** (right) at 80 K. The spectra are deconvoluted into two components indicated as "Comp 1" and "Comp 2."

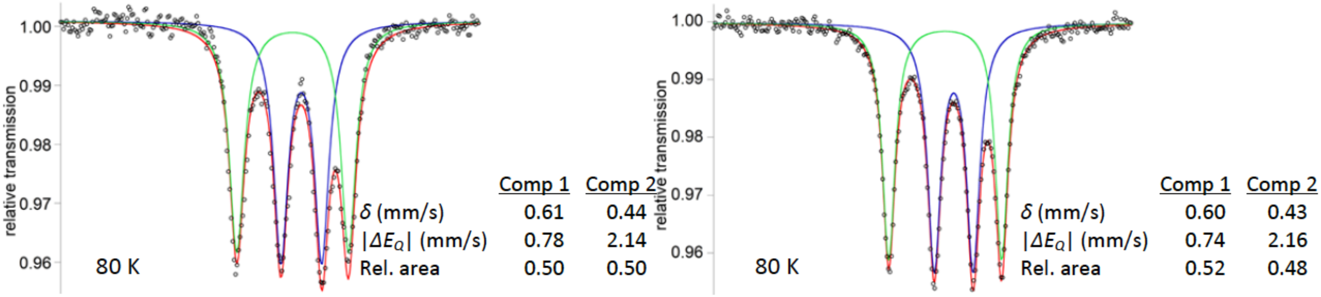

The details of the solid-state behavior are still under study; despite these difficulties, the above data support the description of **1** as having high-spin iron(II) sites.

Magnetic Susceptibility. Magnetic susceptibility data were measured from powder samples of solid **1** in the temperature range 2–300 K using a SQUID susceptometer (MPMS-7, Quantum Design) with a field of 1.0 T. The experimental data were corrected for underlying diamagnetism by use of tabulated Pascal's constants. The susceptibility data, $\chi T(T)$, were simulated with julX for exchange coupled systems.[3] The simulations are based on the usual spin-Hamilton operator for exchange-coupled dimeric compounds with local spins S_i:

$$\hat{H} = -2J\, S_1 \cdot S_2 + \sum_{i=1,2} D_i \left[\hat{S}_{i,z}^2 - {}^{1}\!/_{3}\, S_i(S_i+1) + {}^{E}\!/_{D_i} \left(\hat{S}_{i,x}^2 - \hat{S}_{i,y}^2\right)\right] + \mu_B \vec{B} \cdot g_i \cdot \vec{S}_i \qquad (1)$$

Here J is the exchange coupling constant, g_i are the local electronic g values, and D_i and E/D_i are the axial zero-field splitting and rhombicity parameters, respectively. The magnetic moments in the simulations were obtained from the eigenfunctions $|\psi_i>$ of eq. 1 by using the Hellmann-Feynman theorem,

$$\vec{\mu}_i(\vec{B}) = -\left\langle \psi_i \right| {}^{d\hat{H}}\!\big/_{d\vec{B}} \left| \psi_i \right\rangle$$

Powder summations were done by using a 16-point Lebedev grid. Simulations were attempted with different local spins $S_i = 1$ and $S_i = 2$, but simultaneous fitting of the constant-field (left) and variable-field (bottom) measurements required $S_i = 2$ at both iron sites. The iron sites were assigned equal g and D values in the global fits. Corrections were applied for an S = 0 paramagnetic impurity (14.6%), and for temperature-independent magnetism (203.4 x 10^{-6} emu). The value of D refined to -52 cm^{-1} with $g_{x,y}$ = 2.065 and g_z = 2.154, and E was held at zero for simplicity. The value of J refined to +3.885 cm^{-1}, which is significantly smaller than D implying a high density of low-lying states. Further studies into the electronic structure and the magnetism of **1** will be reported separately.

Figure S5. Magnetic Susceptibility Data.

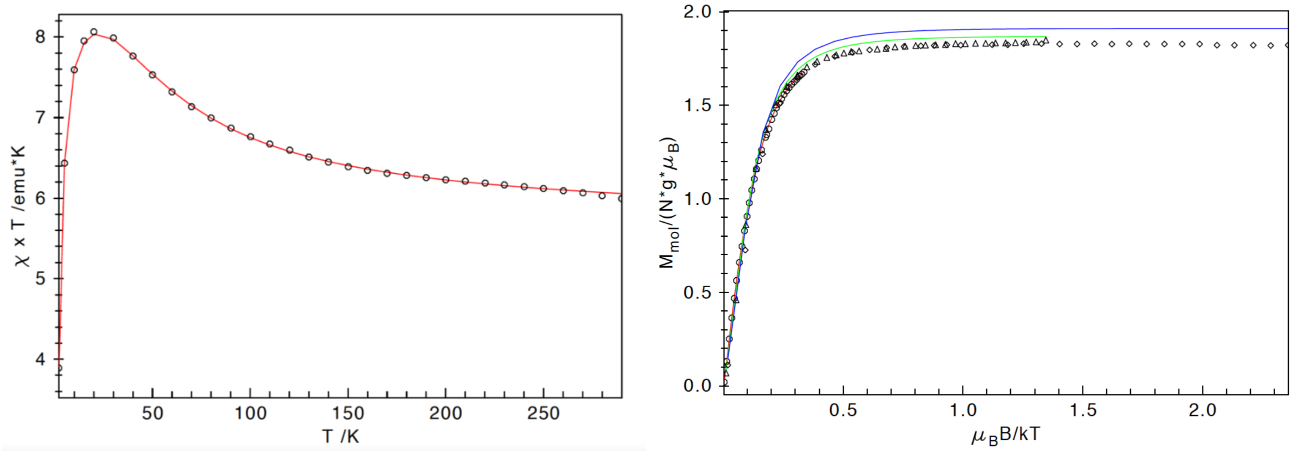

NRVS Measurements. NRVS measurements were conducted at BL09XU at SPring-8, and at 03-ID at the Advanced Photon Source (APS). At SPring-8, principal monochromation at 14.4 keV occurred with a liquid nitrogen cooled (77 K) Si(111) high heat load monochromator (HHLM). It was followed by further monochromation to about 0.8 meV (6.5 cm^{-1}) bandwidth by a three bounce high resolution monochromator (HRM, Ge(4,2,2)x2Si(9,7,5)). The high-resolution X-ray beam excited the ^{57}Fe inside the sample in measurement and a 4-channel avalanche photodiode detector (APD) array was used to detect the direct ^{57}Fe nuclear fluorescence as well as the Fe $K\alpha$ fluorescence via internal conversion. At the APS, a water-cooled diamond(111) double crystal monochromator was used for primary beam monochromation, followed by a 2Si(4,0,0)x2Si(10,6,4) four-bounce HRM to achieve an incident beam with 1.0 cm^{-1} resolution. A 1-cm^2 single element APD was used as detector. At SPring-8 or APS, all measurements were performed with the sample base cooled to <10 K with a liquid helium cooled cold finger cryostat.

The samples were crystalline solids of iron-57 labeled **1** and **1-D$_2$**. The real sample temperature during measurement was roughly 60 ± 20 K, as obtained with PHOENIX during the data NRVS analysis (see below).

To emphasize certain region(s) of interest (ROI) in the NRVS spectra, sectional measurements were performed by scanning longer time per energy position in the ROI than in other regions. In general, both **1** and **1-D$_2$** were scanned from -240 cm^{-1} at SPring-8. In the region from this starting point to 400 cm^{-1}, a time of 5 seconds per energy point was used and 4 scans were taken, leading to 5x4 seconds/point; in the region of 400-600 cm^{-1}, 10x4 seconds/point was used; in the region of 600-1080 cm^{-1}, 15x8 seconds/point was used; for the Fe-H stretching ROI at 1080 – 1600 cm^{-1}, 15x30 seconds/point was used. This single region scan took about 18 hours. To track the resonant peak position, a short $\pm$80 cm^{-1} scan was performed around 0 cm^{-1} after each scan in the Fe-H stretching ROI. At APS, the scans started at -320 cm^{-1} instead, no Fe-H regions were scanned while the scans in the other regions were similar with the ones at SPring-8. The significant changes in acquisition times led to slight discontinuities of signal-to-noise in the combined experimental spectrum in the main text Figure 2 at the interfaces of the ROIs. These discontinuities are not expected to affect our interpretation of the spectrum.

The energy calibration includes the zero position (resonant energy position) alignment and the energy scale calibration. The former was done by aligning the elastic peak for all the scans during the PHOENIX analysis, while the latter was done with a calibration standard. In our measurements, the strong T_2 Fe-Cl asymmetric stretching peak in $[NEt_4][^{57}FeCl_4]$ (at 380 cm^{-1}) was used as the energy calibration standard. For the high-energy region for Fe-H stretching, no energy scale calibration is possible at the moment. We assumed that it has the same energy scale as in the low energy region, where it was calibrated with $[NEt_4][^{57}FeCl_4]$.

The raw NRVS spectra were processed using PHOENIX, as executed through the website www.spectra.tools, to extract the single-phonon ^{57}Fe partial vibrational density of state (PVDOS).[4] Specifically for the high energy Fe-H ROI data (Figure S6), the ROI scans were aligned by their elastic peak positions, then a full low energy spectrum, collected on the same sample at the same beamtime, was used during the data analysis of the Fe-H ROI to approximate the Lamb-Mössbauer factor and spectral normalization which facilitated the final conversion to PVDOS for the high energy region by PHOENIX. The real sample temperatures were derived using the “detailed balance” method in PHOENIX by comparing the ratio of NRVS intensities generated by phonon annihilation and creation.

Figure S6. The combined low energy and high energy region-of-interest (ROI) NRVS scans for ^{57}Fe-labeled **1**, using a logarithmic scale on the *y* axis, showing the summed data and breakdown of the first-, second-, and higher-order contributions to the spectrum. There is a slight discontinuity at 1088 cm^{-1} where the data were joined. This spectrum has had the elastic peak subtracted out and the first moment of the spectrum has been normalized to the recoil energy of ^{57}Fe.

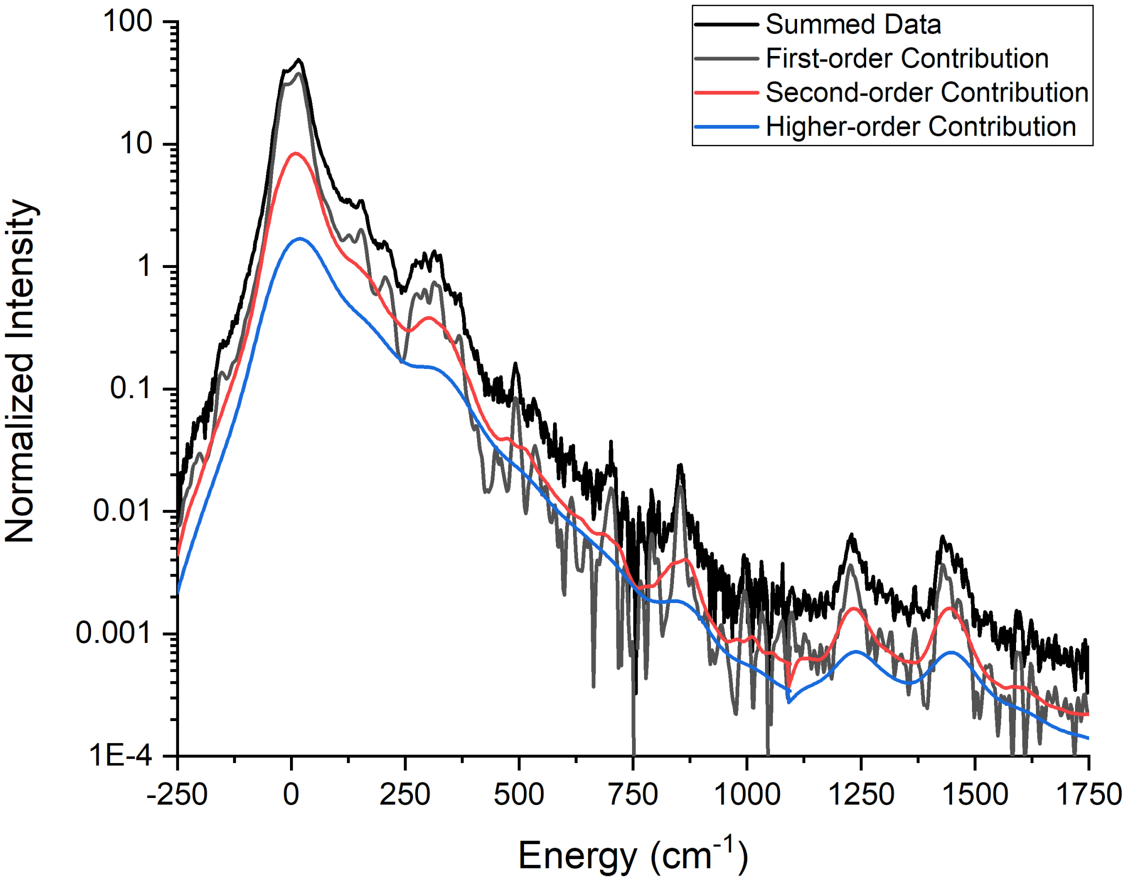

DFT Calculations

Methods. Initial coordinates for DFT modeling were extracted from the published 0.82 Å resolution X-ray structure of **1**.[1] The structure optimization and subsequent normal mode analysis were done using GAUSSIAN 09[5] based on the electron densities exported from single point calculations using JAGUAR 7.9.[6] All the calculations employed spin-unrestricted formalism. Three alternatives on the difference between the total number of α (spin-up) and β (spin-down) electrons have been explored, namely (*i*) $N^\alpha - N^\beta = 0$ designated as '$S = 0$', (*ii*) $N^\alpha - N^\beta = 6$ designated as '$S = 3$', and (*iii*) $N^\alpha - N^\beta = 8$ designated as '$S = 4$'. As detailed below (Table S2, and Figures S9-S10), the $S = 0$ open-shell singlet solution (*i*) bearing a broken-symmetry character[7] was found to give the best agreement with the experimental data. The BP86[8] functional and the LACV3P** basis set as implemented in JAGUAR 7.9 were employed. For the first- and second-row elements, LACV3P** implies 6-311G** triple-zeta basis set including polarization functions. For the Fe atoms, LACV3P** consists of a triple-zeta quality basis set for the outermost core and valence orbitals, and the quasirelativistic Los Alamos effective core potential (ECP) for the innermost electrons.[9] The model environment was considered using a self-consistent reaction field (SCRF) polarizable continuum model and integral equation formalism (IEF-PCM)[10] as implemented in GAUSSIAN 09, with IEF-PCM parameters at their default values for water. Computational schemes were tested (*i*) excluding and (*ii*) including two-body D3 empirical dispersion correction by Grimme *et al* in its original formulation[11] as well as (*iii*) D3 reformulated with Becke-Johnson damping;[12] as explained below (Table S1, and Figures S7-S8), results from scheme (*i*) were optimal and apply to all the DFT data unless otherwise mentioned. Based on the normal mode outputs from GAUSSIAN 09, an in-house Q-SPECTOR program successfully applied previously[13] was utilized to generate the normal mode composition factors[14] and PVDOS for the 2×^{57}Fe iron nuclei (which is simulated NRVS), and as well PVDOS for the 2×H^-/D^- bridging hydride nuclei (for which no experimental complement is available). The resolution of the observed NRVS spectra was accounted by convolution of the computed intensities with a full width at half maximum (FWHM) = 16 cm^{-1} Lorentzian for the higher intensity ^{57}Fe-PVDOS bands <460 cm^{-1}, and with FWHM = 24 cm^{-1} Lorentzian for the lower intensity bands >460 cm^{-1}. Empirical scaling of the calculated frequencies was not applied. Superposition of the DFT-optimized structures onto their X-ray reference in Figures 1, S7, and S9 was achieved through pairwise minimization of the root-mean-square deviation (RMSD) between positions of six (2×Fe and 4×N) nuclei labeled in Figures S7 and S9.

On the Role of Dispersion Correction. Inclusion of empirical dispersion correction at the level of structure optimization and subsequent normal mode analysis has been presently examined for **1** using schemes (*i*)-(*iii*) as described in the DFT methods; all three computational schemes are frequently applied in modern DFT studies. The results from these alternatives are designated respectively as 'no dispersion', 'D3', and 'D3BJ' and are collected in Table S1 and Figures S7-S8.

As can be inferred from Figure S7, inclusion of dispersion interaction in schemes D3(BJ) generally gives better alignment of the four dimethylphenyl groups with their original (non-optimized) X-ray reference positions, as compared to the scheme lacking the dispersion correction. At the same time, Table S1 indicates that the D3(BJ) schemes lead to an over-compressed core of **1** with the Fe–Fe and Fe–N distances shorter by ~0.1 and 0.04-0.07 Å, respectively, when compared to the X-ray structure. Particularly on the Fe–Fe distance, the scheme that excludes the empirical dispersion performs noticeably better. The Fe–H distances delivered by all three schemes are ~0.1 Å longer than those in the X-ray structure; metal-hydride distances from X-ray data analysis are however commonly problematic.[15]

Figure S8 further compares the ^{57}Fe-PVDOS spectra of **1** observed by NRVS spectra calculated following the three (*i*)-(*iii*) schemes. Inclusion of dispersion in the D3(BJ) schemes enhances the intensities in the ~350-450 cm^{-1} area where several modes of Fe–Fe stretching character are present; see animated normal modes at 371 and 394 cm^{-1} available in Supporting Information separately. D3(BJ) schemes also noticeably blue-shift all in-plane Fe–H^{-}/D^{-}–Fe modes >880 cm^{-1} by up to ~90 cm^{-1} for the high-end Fe–H^{-}–Fe modes (see these modes characterized in the main text Figure 2 and depicted in Scheme 1). The discussed band upshifts introduce deviation from the observed NRVS spectra and can be attributed to the Fe–Fe distance becoming markedly compressed when the dispersion is included, as explained above. Notably, expansion of Fe–Fe distances has been identified as a key structural parameter in mapping gradual red-shifts of NRVS bands in [3Fe–4S]$^{1+}$/[3Fe–4S]^{0}/[4Fe–4S]$^{2+}$/[4Fe–4S]$^{1+}$ iron-sulfur clusters from *Pyrococcus furiosus* ferredoxin.[16] Finally, NRVS bands in the ~490-880 cm^{-1} region that largely emerge from mixed vibrations of the substituent groups (and translated to the ^{57}Fe nuclei displacements via the N ligands), are somewhat better reproduced by the D3(BJ) schemes.

In summary, with our focus on the iron-hydride vibrational motion, the DFT scheme (*i*) that lacks dispersion correction has been presently selected as the best fit; we additionally note only a minor sensitivity of the dispersion-corrected results to the specific damping function applied (D3 vs D3BJ). Exclusion of dispersion correction in attempt to accurately reproduce specifically the iron-hydride vibrational frequencies from NRVS goes in line with previous experience.[17][18]

Table S1. Metal-metal and metal-ligand internuclear distances (Å) in species **1** from X-ray crystallography data analysis[1] and DFT optimizations (*i*) excluding (no dispersion) and (*ii*) including two-body D3 dispersion correction (D3), as well as (*iii*) D3 including Becke-Johnson damping (D3BJ).[a]

	Fe_1–Fe_2	Fe–H[b]				Fe–N			
		Fe_1–H_1	Fe_1–H_2	Fe_2–H_1	Fe_2–H_2	Fe_1–N_{1A}	Fe_1–N_{1B}	Fe_2–N_{2A}	Fe_2–N_{2B}
X-ray	**2.50**	**1.57**	**1.58**	**1.58**	**1.57**	**1.93**	**1.93**	**1.93**	**1.93**
DFT no dispersion[c]	2.49	1.68	1.69	1.68	1.69	1.89	1.91	1.89	1.91
DFT D3	2.39	1.66	1.66	1.66	1.66	1.86	1.87	1.87	1.89
DFT D3BJ	2.40	1.66	1.67	1.67	1.67	1.86	1.87	1.86	1.88

[a] The atom labels and text color codes correspond to those used in Figures S7-S8.
[b] The experimental Fe–H distances are expected to suffer from systematic shortening, as well-known from X-ray crystallography studies.[15]
[c] The best-fit DFT model.

Figure S7. Structures of species **1** from X-ray crystallography data[1] overlaid with DFT models optimized (*i*) excluding (no dispersion, the representative DFT structure shown as well in Figure 1 of the main text) and (*ii*) including two-body D3 dispersion correction (D3), as well as (*iii*) D3 including Becke-Johnson damping (D3BJ). Hydrogen atoms except the two bridging hydrides are omitted for clarity. Two views are given.

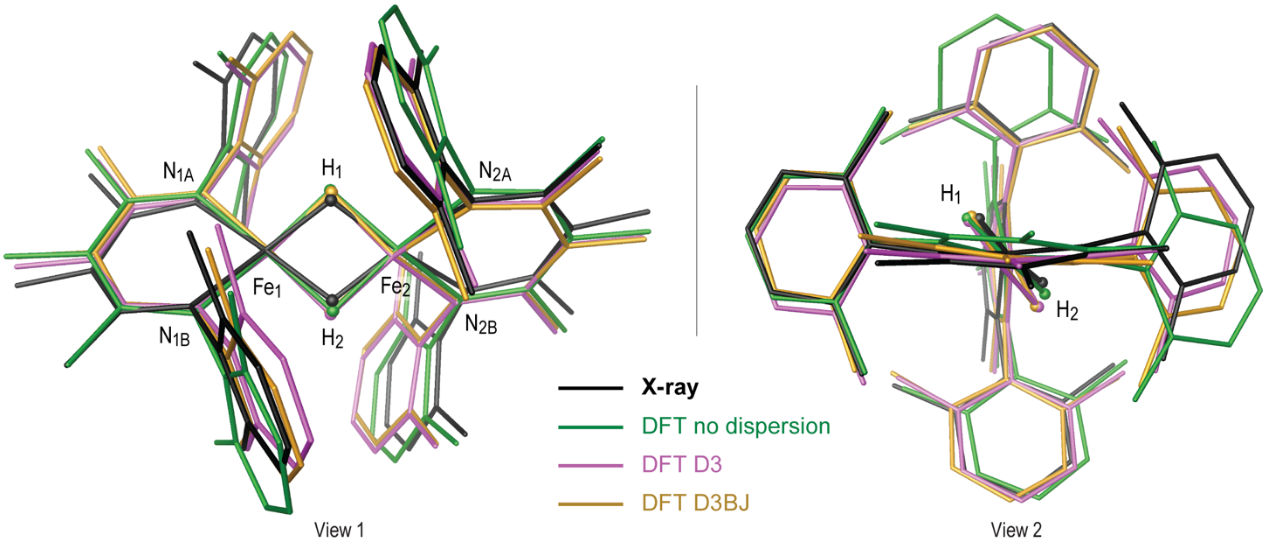

Figure S8. ^{57}Fe-PVDOS spectra of **1** (b) and **1-D$_2$** (a) characterized by NRVS experiments and DFT calculations (*i*) excluding (no dispersion, the representative DFT spectra shown as well in Figure 2b of the main text) and (*ii*) including two-body D3 dispersion correction (D3), as well as (*iii*) D3 including Becke-Johnson damping (D3BJ). Only the NRVS band positions associated with key iron-hydride vibrational modes (see the main text Scheme 1) are labeled.

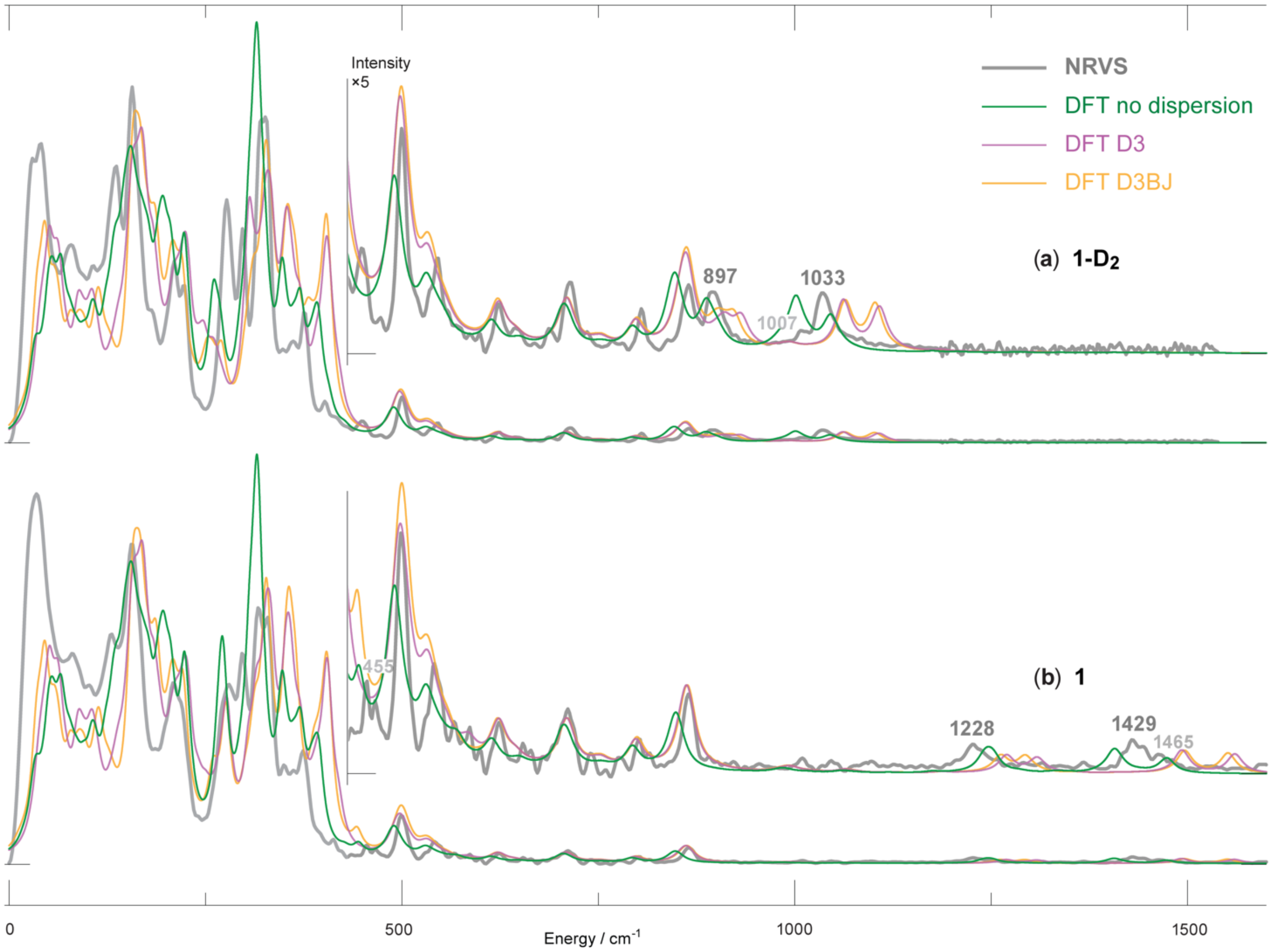

Electronic Structure Alternatives. Three alternatives on the electronic structure of species **1** have been presently examined. The results from these alternatives called ‘*S* = 0/3/4’ are collected in Table S2 and Figures S9-S10. Bearing in mind that the main spin quantum number *S* is generally not well-defined in the single-determinant DFT approach, the designation of the states merely reflects a difference in the total number of α (spin-up) and β (spin-down) electrons as described in the DFT methods. Notably, the ‘*S* = 0’ solution is equivalent to the ‘no dispersion’ DFT scheme covered in the previous section.

The ‘*S* = 0’ and ‘*S* = 4’ alternatives initially aimed to represent anti- and ferromagnetic couplings of the two Fe^{2+} centers, both in their high-spin *S* = 2 states based on the Mössbauer spectroscopy measurements; the ‘*S* = 3’ solution has been initially converged using the densities from the ‘*S* = 4’ solution. Given the large zero-field splitting (see the magnetic susceptibility data) we note that the current DFT methodology should serve as an approximation of the electronic structure; more complicated schemes are however not feasible to apply with a molecule of this size when the vibrational analysis is in focus.

The structures of **1** optimized using the electronic configurations ‘*S* = 0/3/4’ are shown in Figure S9, and the core structural parameters are in Table S2. Both the ‘*S* = 0’ and ‘*S* = 3’ structures provide a reasonable fit to the metrical parameters in the X-ray structure. The ‘*S* = 3’ solution delivers a superior accuracy in positioning of the dimethylphenyl groups, and produces metal–metal/ligand distances somewhat longer than those from the ‘*S* = 0’ solution. In contrast, the high-spin solution ‘*S* = 4’ results in a significantly more expanded core of the complex, with the Fe–Fe/N ligand distances overestimated by ~0.1 Å as compared to the X-ray reference. The ‘*S* = 4’ structure optimization as well effects in a noticeable deviation of the two diketiminate ring planes from their approximately normal (~90°) orientation seen in the X-ray structure and from other optimizations (see Figure S9, View 2).

The ^{57}Fe-PVDOS vibrational spectra of **1** observed by NRVS vs those calculated based on the three ‘*S* = 0/3/4’ alternatives are shown in Figure S10. In line with the above discussion on the dispersion effects and earlier results[16] on polynuclear Fe systems, we find that the Fe–Fe distance plays an important role in defining the calculated ^{57}Fe-PVDOS (simulated NRVS) features: its expansion in the ‘*S* = 4’ structure leads to significant depopulation of the intensities in the ~300-400 cm^{-1} area, as well as red-shifts of the Fe–H/D–Fe band positions. The hydride bands are also clearly worse reproduced by the ‘*S* = 3’ alternative, as compared to those from the ‘*S* = 0’ model.

In summary, the broken-symmetry[7] solution ‘*S* = 0’ has been presently selected as the best fit to the NRVS data. Though the different models examined here produced modifications in the quantitative aspects of the calculated NRVS spectra, the qualitative similarities between all of the calculated spectra lend confidence to the assignments of the isotope-sensitive bands in the NRVS spectra, as given in the text.

Table S2. Metal-metal and metal-ligand internuclear distances (Å) in species **1** from X-ray crystallography data analysis[1] and DFT optimizations employing electronic structures designated as *S* = 0, 3, and 4.[a]

	Fe_1–Fe_2	Fe–H[b]				Fe–N			
		Fe_1–H_1	Fe_1–H_2	Fe_2–H_1	Fe_2–H_2	Fe_1–N_{1A}	Fe_1–N_{1B}	Fe_2–N_{2A}	Fe_2–N_{2B}
X-ray	**2.50**	**1.57**	**1.58**	**1.58**	**1.57**	**1.93**	**1.93**	**1.93**	**1.93**
DFT *S* = 0[c]	2.49	1.68	1.69	1.68	1.69	1.89	1.91	1.89	1.91
DFT *S* = 3	2.51	1.70	1.70	1.66	1.66	1.96	1.95	1.94	1.95
DFT *S* = 4	2.57	1.81	1.81	1.78	1.78	2.02	2.00	2.02	2.00

[a] The atom labels and text color codes correspond to those used in Figures S9-S10.
[b] The experimental Fe–H distances are expected to suffer from systematic shortening, as well-known from X-ray crystallography studies.[15]
[c] The best-fit DFT model.

Figure S9. Structures of species **1** from X-ray crystallography data[1] overlaid with DFT models optimized employing electronic structures designated as $S = 0$ (the representative DFT structure shown as well in Figure 1 of the main text), 3, and 4. Hydrogen atoms except the two bridging hydrides are omitted for clarity. Two alternative views are given.

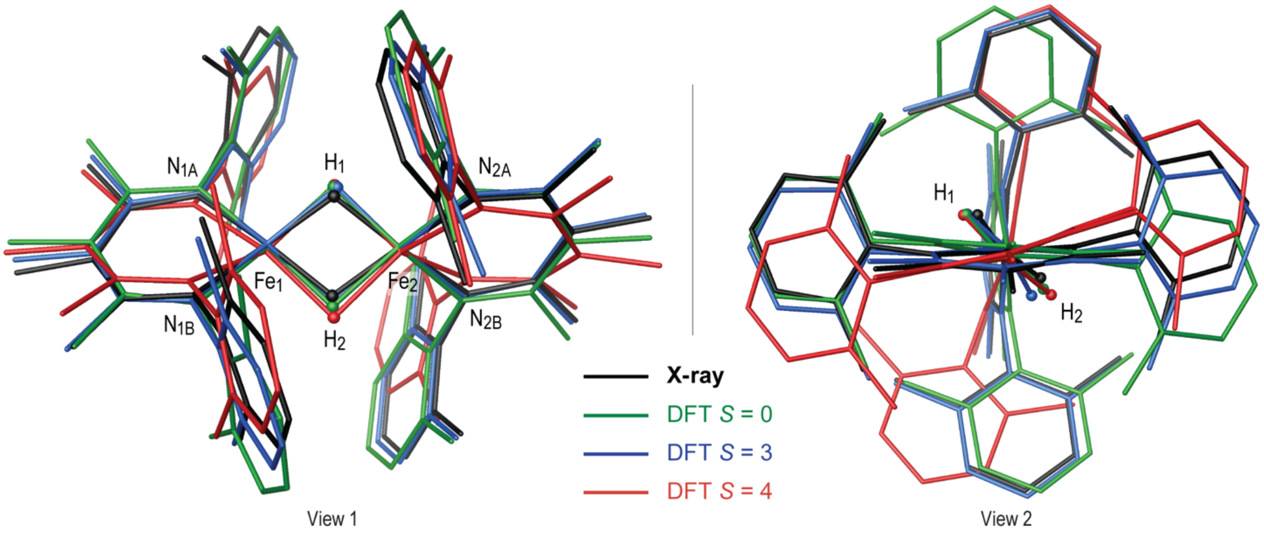

Figure S10. ^{57}Fe-PVDOS spectra of **1** (b) and **1-D$_2$** (a) characterized by NRVS experiments and DFT calculations employing electronic structures designated as $S = 0$ (the best-fit DFT spectra shown as well in Figure 2b of the main text), 3, and 4. Only the NRVS band positions associated with key iron-hydride vibrational modes (see the main text Scheme 1) are labeled.

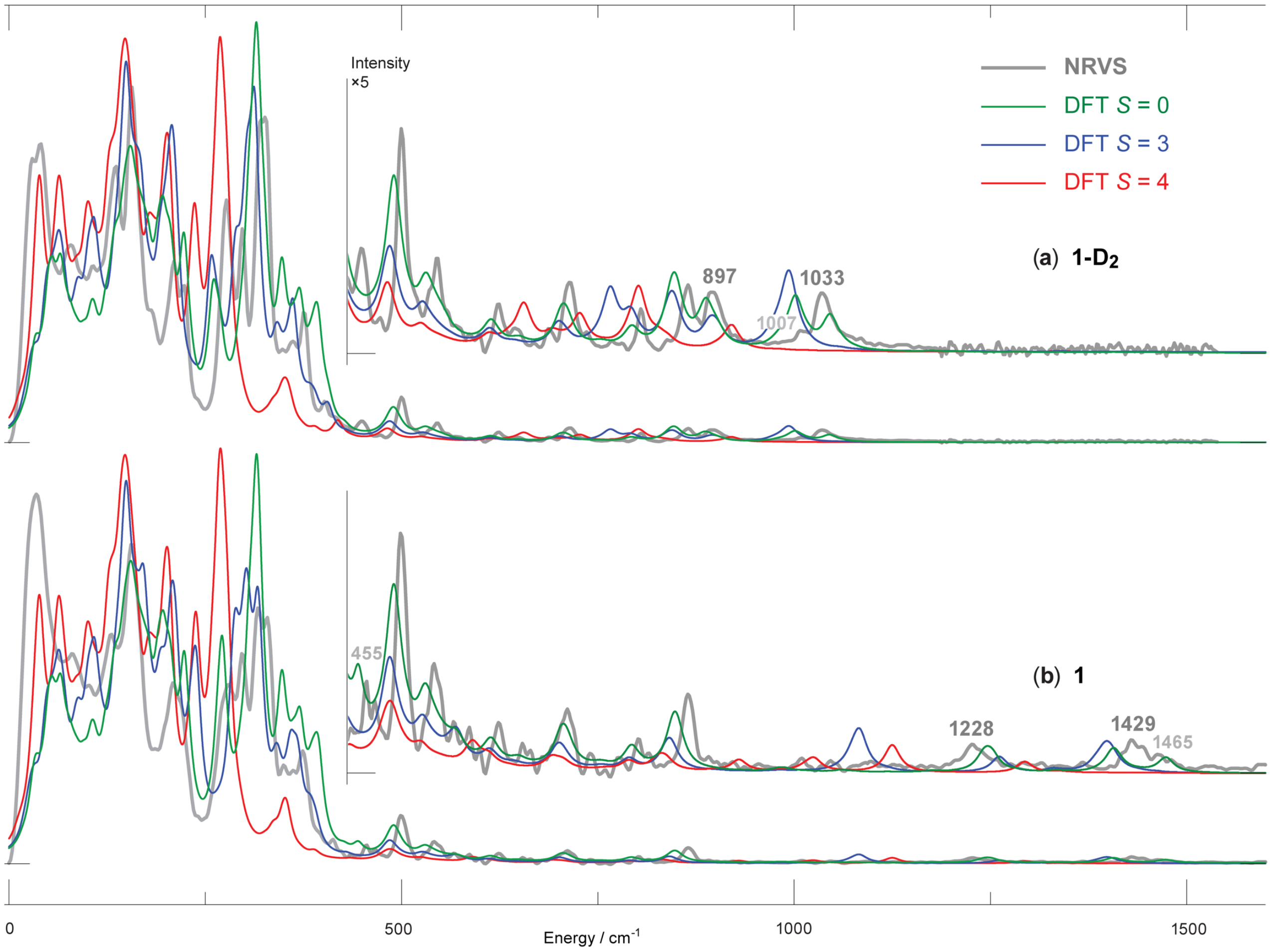

Hydride Vibrations in a D_2-symmetric $L_2Fe(\mu\text{-}H)_2FeL_2$ System. In the X-ray and best-fit DFT structures of **1**, the two diketiminate ring planes are at ~90° to each other, and the $Fe(\mu\text{-}H)_2Fe$ metal-hydride plane bisects this angle, see e.g. Figure S7 or S9, View 2; while the system is not rigorously symmetric, the $N_2Fe(\mu\text{-}H)_2FeN_2$ metal-ligand core has an apparent link to the D_2 point group. To strengthen this connection, a minimalistic model of **1** called $\mathbf{1_M}$ has been computationally considered, which is a $H_2Fe(\mu\text{-}H)_2FeH_2$ di-iron(II) hexahydride, see Figure S11. Employing molecular symmetry routine in GAUSSIAN 09, model $\mathbf{1_M}$ has been structurally optimized in the D_2 symmetry framework. Analogously to the main system **1**, vibrational spectra were then calculated for the bridging hydride (H_1 and H_2 in Figure S11, left) isotopologues having $(\mu\text{-}H)_2$ and $(\mu\text{-}D)_2$, and further referred to as $\mathbf{1_M}$ and $\mathbf{1_M\text{-}D_2}$. To reinforce the relationship to **1** for the vibrational analysis, the four terminal hydride nuclei (H_{1A}, H_{1B}, H_{2A}, and H_{2B} in Figure S11, left) of $\mathbf{1_M}$ were set to a fictitious ^{14}H isotope that mimics the atomic mass of the corresponding nitrogen nuclei in **1** (N_{1A}, N_{1B}, N_{2A}, and N_{2B} in Figures S7 or S9); this setup avoids strong vibrational coupling between the terminal and bridging ligands.

$\mathbf{1_M}$ produces a simple vibrational spectrum that has six distinct normal modes for the $2\times H^-/D^-$ bridging hydrides, with two modes per each principal axis of symmetry; the four $Fe(\mu\text{-}H)_2Fe$ in-plane stretching/bending modes display hydride displacements along the `X` and `Y` axes, and the two out-of-plane wagging modes are along the `Z` axis, as shown in Figures S11-12 and Scheme S1. These vibrations in $\mathbf{1_M}$ are essentially equivalent to the prominent hydride modes in **1**, discriminated from other modes by means of $2\times H^-/D^-$-specific PVDOS (Figures S12b or 2c). In summary, the characters and vibrational energies of the bridging hydride modes are strongly correlated in systems $\mathbf{1_M}$ (D_2 symmetry) and **1** (formally C_1 symmetry). Vibrational spectroscopy selection rules are therefore applicable here, which predict that the highest-frequency mode of *A* symmetry calculated for $\mathbf{1/1\text{-}D_2}$ at respectively 1474/1046 cm^{-1} (and associated with the NRVS bands observed at 1465/1033 cm^{-1}, see the main text Scheme 1) is IR inactive.

Figure S11. Minimalistic hexahydride DFT model $\mathbf{1_M}$ = $H_2Fe(\mu\text{-}H)_2FeH_2$ optimized in the D_2 symmetry framework and shown in its standard orientation (left), along with the character table for the D_2 point group (right).

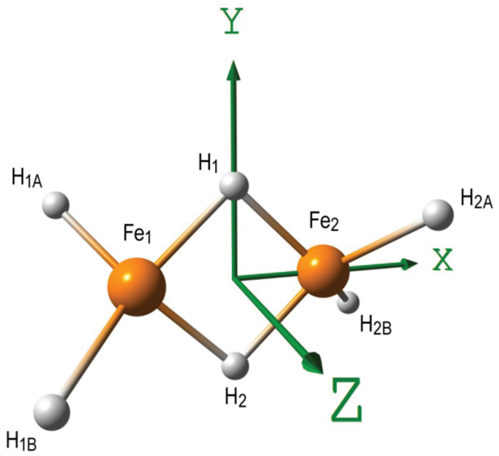

$\mathbf{1_M}$

D_2	*E*	C_2(z)	C_2(y)	C_2(x)
A	1	1	1	1
B_1	1	1	-1	-1
B_2	1	-1	1	-1
B_3	1	-1	-1	1

Scheme S1. Arrow-style graphic representation of the principal bridging hydride normal modes along with their frequencies (in units of cm^{-1}) computed using DFT and matched (top-to-bottom) for **1** (right) vs its minimalistic model **1_M** bearing D_2 point-group symmetry (left). The frequency data for the H/D-variants **1**/**1-D_2** and **1_M**/**1_M-D_2** are correspondingly in blue/red. For **1**, only the core Fe sites and their first-shell ligand atoms are shown. For **1_M**, normal mode symmetries are characterized using their D_2 irreducible representations. For **1**, see the main text Scheme 1 matching the shown modes to observed NRVS bands, and the animated vibrational modes are available in Supporting Information separately.

1_M				**1**		
	D_2 irrep	ν (**1_M**)	ν (**1_M-D_2**)		ν (**1**)	ν (**1-D_2**)
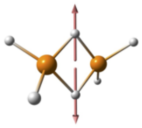	***A***	1323	942	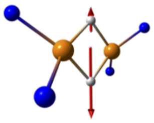	1474	1046
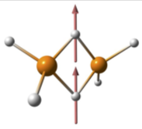	**B_2**	1285	918	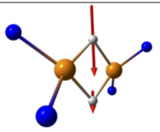	1405	1002
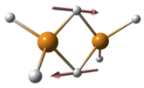	**B_1**	1239	881	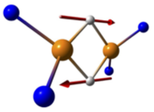	1252	886
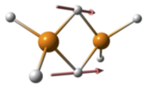	**B_3**	1149	821	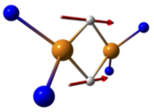	1243	888
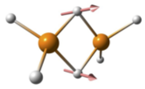	**B_1**	276	215	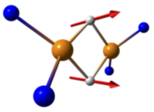	570	407
	**B_3**	224	207	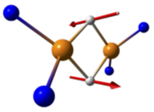	445	326

Figure S12. 2×H$^-$/D$^-$-specific PVDOS stick-style spectra of **1_M** (a) and **1** (b) from DFT calculations, which quantify the bridging hydride nuclei motion. The H/D-variant **1**/**1-D_2** and **1_M**/**1_M-D_2** data are correspondingly in blue/red. The **1_M**-to-**1** mode equivalences are indicated by the broken lines. Vibrational mode assignments (bottom) are given with respect to the Fe(μ-H)$_2$Fe core. Spectra in (b) repeat the main text Figure 2c.

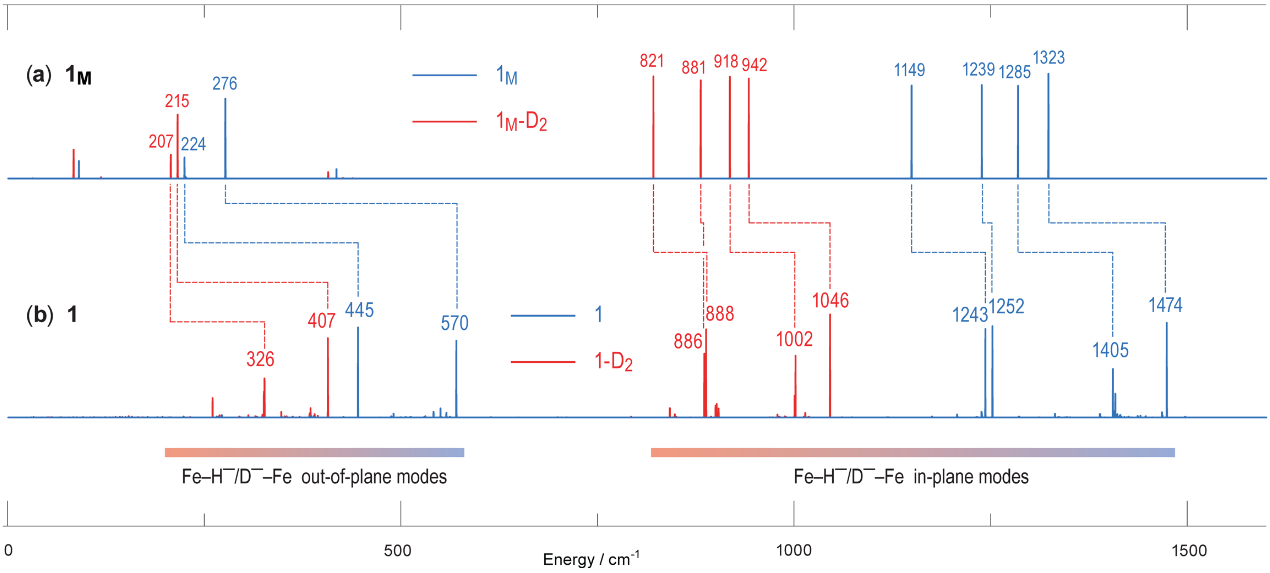

References

[1] M. M. Rodriguez, E. Bill, W. W. Brennessel, P. L. Holland, *Science* **2011**, *334*, 780-783.

[2] a) R. A. Heintz, T. G. Neiss, K. H. Theopold, *Angew. Chem.* **1994**, *106*, 2389-2391; b) T. R. Dugan, E. Bill, K. C. MacLeod, W. W. Brennessel, P. L. Holland, *Inorg. Chem.* **2014**, *53*, 2370-2380.

[3] julX is available from E. Bill at ebill@gwdg.de.

[4] W. Sturhahn, T. S. Toellner, E. E. Alp, X. Zhang, M. Ando, Y. Yoda, S. Kikuta, M. Seto, C. W. Kimball, B. Dabrowski, *Phys. Rev. Lett.* **1995**, *74*, 3832-3835.

[5] M. J. Frisch, G. W. Trucks, H. B. Schlegel, G. E. Scuseria, M. A. Robb, J. R. Cheeseman, G. Scalmani, V. Barone, B. Mennucci, G. A. Petersson, H. Nakatsuji, M. Caricato, X. Li, H. P. Hratchian, A. F. Izmaylov, J. Bloino, G. Zheng, J. L. Sonnenberg, M. Hada, M. Ehara, K. Toyota, R. Fukuda, J. Hasegawa, M. Ishida, T. Nakajima, Y. Honda, O. Kitao, H. Nakai, T. Vreven, J. A. Montgomery, Jr., J. E. Peralta, F. Ogliaro, M. Bearpark, J. J. Heyd, E. Brothers, K. N. Kudin, V. N. Staroverov, R. Kobayashi, J. Normand, K. Raghavachari, A. Rendell, J. C. Burant, S. S. Iyengar, J. Tomasi, M. Cossi, N. Rega, J. M. Millam, M. Klene, J. E. Knox, J. B. Cross, V. Bakken, C. Adamo, J. Jaramillo, R. Gomperts, R. E. Stratmann, O. Yazyev, A. J. Austin, R. Cammi, C. Pomelli, J. W. Ochterski, R. L. Martin, K. Morokuma, V. G. Zakrzewski, G. A. Voth, P. Salvador, J. J. Dannenberg, S. Dapprich, A. D. Daniels, Ö. Farkas, J. B. Foresman, J. V. Ortiz, J. Cioslowski, D. J. Fox, *Gaussian 09, Revision D.01, Gaussian Inc., Wallingford CT, 2009*.

[6] J. F. Hartwig, *Organotransition Metal Chemistry*, University Science Books, Sausalito, CA, **2010**.

[7] a) L. Noodleman, *J. Chem. Phys.* **1981**, *74*, 5737-5743; b) L. Noodleman, D. A. Case, *Adv. Inorg. Chem.* **1992**, *38*, 423-470.

[8] a) A. D. Becke, *Phys. Rev. A* **1988**, *38*, 3098-3100; b) J. P. Perdew, *Phys. Rev. B* **1986**, *33*, 8822-8824.

[9] a) R. Krishnan, J. S. Binkley, R. Seeger, J. A. Pople, *J. Chem. Phys.* **1980**, *72*, 650-654; b) A. D. McLean, G. S. Chandler, *J. Chem. Phys.* **1980**, *72*, 5639-5648.

[10] J. Tomasi, B. Mennucci, R. Cammi, *Chem. Rev.* **2005**, *105*, 2999-3093.

[11] S. Grimme, J. Antony, S. Ehrlich, H. Krieg, *J. Chem. Phys.* **2010**, *132*, 154104.

[12] S. Grimme, S. Ehrlich, L. Goerigk, *J. Comput. Chem.* **2011**, *32*, 1456-1465.

[13] a) D. Mitra, S. J. George, Y. S. Guo, S. Kamali, S. Keable, J. W. Peters, V. Pelmenschikov, D. A. Case, S. P. Cramer, *J. Am. Chem. Soc.* **2013**, *135*, 2530-2543; b) L. F. Yan, V. Pelmenschikov, C. H. Dapper, A. D. Scott, W. E. Newton, S. P. Cramer, *Chem. Eur. J* **2012**, *18*, 16349-16357; c) V. Pelmenschikov, Y. Guo, H. Wang, S. P. Cramer, D. A. Case, *Faraday Disc.* **2011**, *148*, 409-420; d) D. Mitra, V. Pelmenschikov, Y. S. Guo, D. A. Case, H. X. Wang, W. B. Dong, M. L. Tan, T. Ichiye, F. E. Jenney, M. W. W. Adams, Y. Yoda, J. Y. Zhao, S. P. Cramer, *Biochemistry* **2011**, *50*, 5220-5235.

[14] T. Petrenko, W. Sturhahn, F. Neese, *Hyperfine Interactions* **2008**, *175*, 165-174.

[15] W. Massa, *Crystal Structure Determination*, 2nd ed., Springer, New York, **2000**.

[16] L. Lauterbach, L. B. Gee, V. Pelmenschikov, F. E. Jenney, S. Kamali, Y. Yoda, M. W. W. Adams, S. P. Cramer, *Dalton Trans.* **2016**, *45*, 7215-7219.

[17] a) E. J. Reijerse, C. C. Pham, V. Pelmenschikov, R. Gilbert-Wilson, A. Adamska-Venkatesh, J. F. Siebel, L. B. Gee, Y. Yoda, K. Tamasaku, W. Lubitz, T. B. Rauchfuss, S. P. Cramer, *J. Am. Chem. Soc.* **2017**, *139*, 4306-4309; b) H. Ogata, T. Kramer, H. Wang, D. Schilter, V. Pelmenschikov, M. van Gastel, F. Neese, T. B. Rauchfuss, L. B. Gee, A. D. Scott, Y. Yoda, Y. Tanaka, W. Lubitz, S. P. Cramer, *Nature Commun.* **2015**, *6*, 7890.

[18] V. Pelmenschikov, J. A. Birrell, C. C. Pham, N. Mishra, H. Wang, C. Sommer, E. Reijerse, C. P. Richers, K. Tamasaku, Y. Yoda, T. B. Rauchfuss, W. Lubitz, S. P. Cramer, *J. Am. Chem. Soc.* **2017**, *139*, 16894-16902.